The Journal of Chemical Physics

# Complete characterization of the 3*p* Rydberg complex of a molecular ion: $MgAr^+$. II. Global analysis of the $A^+\ ^2\Pi$ and $B^+\ ^2\Sigma^+$ ($3p_{\sigma,\pi}$) states

Cite as: J. Chem. Phys. **153**, 074311 (2020); https://doi.org/10.1063/5.0015608
Submitted: 29 May 2020 . Accepted: 19 July 2020 . Published Online: 20 August 2020

Matthieu Génévriez, Dominik Wehrli, and Frédéric Merkt



The Journal of Chemical Physics ARTICLE scitation.org/journal/jcp

# Complete characterization of the 3*p* Rydberg complex of a molecular ion: $MgAr^+$. II. Global analysis of the $A^+{}^2\Pi$ and $B^+{}^2\Sigma^+$ ($3p_{\sigma,\pi}$) states

Cite as: J. Chem. Phys. 153, 074311 (2020); doi: 10.1063/5.0015608
Submitted: 29 May 2020 • Accepted: 19 July 2020 •
Published Online: 20 August 2020



Matthieu Génévriez, Dominik Wehrli, and Frédéric Merkt[a]

## AFFILIATIONS

Laboratory of Physical Chemistry, ETH Zurich, CH-8093 Zurich, Switzerland

[a]Author to whom correspondence should be addressed: merkt@phys.chem.ethz.ch

## ABSTRACT

We report a global study of the 3*p* Rydberg complex of the $MgAr^+$ molecular ion. High-resolution spectroscopic data on the two spin–orbit components of the $A^+$ electronic state were obtained by isolated-core multiphoton Rydberg-dissociation spectroscopy up to vibrational levels as high as $v' = 29$, covering more than 90% of the potential wells. Accurate adiabatic potential-energy functions of the $A^+$ and $B^+$ states, which together form the 3*p* Rydberg complex, were obtained in a global direct-potential-fit analysis of the present data and the extensive data on the $B^+$ state reported in Paper I [D. Wehrli *et al.*, J. Chem. Phys. **153**, 074310 (2020)]. The dissociation energies of the $B^+$ state, the two spin–orbit components of the $A^+$ state, and the $X^+$ state of $MgAr^+$ are obtained with uncertainties (1 $cm^{-1}$) more than two orders of magnitude smaller than in previous studies.



## I. INTRODUCTION

The complete experimental characterization of molecular Rydberg states necessitates the measurement of spectra of a large number of states of different principal and angular-momentum quantum numbers and, for each of them, of a large number of rotational and vibrational levels, extending from the vibrational ground state to levels close to the dissociation threshold.[1–10] This task is particularly difficult for cations because of the low densities in which they can be produced compared to neutral species and the larger photon energies required for electronic excitation. In addition, diatomic cations produced by conventional ion sources are, in most cases, in their vibrational ground state, which restricts the accessible vibrational levels of electronically excited states to those having significant Franck–Condon overlap with the ground vibronic state. For this reason, hardly any systematic studies of the Rydberg states of molecular cations have been reported so far. This situation is in stark contrast to that prevailing for the ground and low-lying valence states of cations, for which many examples of detailed characterization by high-resolution spectroscopy are known; see, e.g., Refs. 11–20 and references therein.

We showed recently, with the example of $MgAr^+$, that *state-selected* cations can be prepared in a wide range of vibrational levels of the electronic ground state by photoexcitation of neutral molecules to high-lying Rydberg states.[21] For sufficiently large values of the principal quantum number ($n \geq 100$) or orbital-angular-momentum quantum number of the Rydberg electron, the ionic core of the Rydberg molecule can be considered as *isolated* from the Rydberg electron and behaves as the bare ion. With the method of isolated-core multiphoton Rydberg-dissociation (ICMRD) spectroscopy,[21] the ionic core is first prepared in a selected vibrational level of the electronic ground state and subsequently photodissociated in a multiphoton process. ICMRD spectroscopy opens up the possibility of systematically studying a broad range of vibrational levels belonging to electronically excited states of molecular ions in a background-free manner. As a demonstration, we have recorded spectra of the $3p_\sigma$ $B^+(v')$ state of $MgAr^+$ starting from the ground vibrational level ($v' = 0$) and extending to the dissociation limit and beyond.[22] The present article extends this study to the $3p_\pi$ component, which consists of the two $\Omega = 1/2$ and $\Omega = 3/2$ spin–orbit components of the $A^+$ state.

The four lowest electronic states of $MgAr^+$ follow the structure of the 3*s* and 3*p* orbitals of the $Mg^+$ ion and thus possess a Rydberg character in the sense of Mulliken[23] (see Fig. 2 in Ref. 22). The $3s_\sigma$ $X^+{}^2\Sigma^+$ ground state correlates with the $Ar(^1S_0) + Mg^+(^2S_{1/2})$ dissociation asymptote, whereas the 3*p* complex consists of three excited electronic states correlating with the $Ar(^1S_0) + Mg^+(^2P_{1/2,3/2})$ dissociation limits. At short internuclear distances, two of these states can be regarded as the two spin–orbit components of the $3p_\pi$ $A^+{}^2\Pi_{\Omega'=1/2,3/2}$ state, and the third can be regarded as the $3p_\sigma$ $B^+{}^2\Sigma^+$ state. They will be denoted as $A^+_{1/2}$, $A^+_{3/2}$, and $B^+$ below. The low-lying vibrational levels ($v' \leq 14$) of the two spin–orbit components of the $A^+$ state were first observed in the pioneering work of Duncan and co-workers,[24–26] and the rotational constant of the $v' = 5$ state was determined in a subsequent high-resolution study.[27] The spectra of the $A^+(v' = 0, 1, 5) \leftarrow X^+(v'' = 3)$ vibrational bands with a partially resolved rotational structure were also observed recently by ICMRD spectroscopy.[21] In parallel, the $A^+$ state of $MgAr^+$ was investigated theoretically in Refs. 22 and 28–35. The rovibrational structure of the $B^+$ state has first been measured in the study reported in Paper I.[22]

The present article reports high-resolution spectroscopic data on the $A^+$ state of $MgAr^+$ obtained by ICMRD spectroscopy. Vibrational levels as high as $v' = 29$ have been observed, and the rotational structure of the vibrational bands could be partially resolved up to $v' = 28$. The data cover more than 90% the potential wells of each of the two spin–orbit components of the $A^+$ state. Combined with the data reported on the $B^+$ state in Paper I,[22] which cover its entire potential depth, the new data provide complete and detailed information on the 3*p* Rydberg complex of $MgAr^+$. From the experimental results, high-accuracy adiabatic potential-energy functions were determined for the three electronic states using a direct-potential-fit technique[36] combined with a model describing the spin–orbit interaction at the relevant internuclear distances. A similar approach was previously used to describe the ground and first electronically excited states of the homonuclear rare-gas dimers.[37–41]

## II. EXPERIMENT

The experimental setup and the technique of ICMRD spectroscopy used in the present work were described in detail in Refs. 21 and 42. Briefly, a molecular beam containing rotationally and vibrationally cold MgAr molecules is first formed in a pulsed laser-ablation supersonic-expansion source. MgAr molecules are, for their vast majority, in the metastable $Mg(3s3p)Ar$ $a\,^3\Pi_0(v = 0)$ state, and their rotational temperature is estimated to be of the order of 10 K for the data presented below. After passing through a 3-mm-diameter skimmer located 8 cm downstream from the source, the molecular beam enters the photoexcitation chamber, where it is intersected at right angles by the beams of two pulsed dye lasers pumped by the second harmonic of a Nd:YAG laser.

The first laser pulse, corresponding to the frequency-tripled output of the first dye laser and with a wave number tunable in the range from 39 000 $cm^{-1}$ to 39 500 $cm^{-1}$, excites the neutral MgAr molecules from the metastable $a\,^3\Pi_0$ state to high-lying Rydberg states with principal quantum numbers $n \simeq 120$ lying just below a specific $X^+{}^2\Sigma^+(v'')$ ionization threshold of MgAr. The second laser pulse, corresponding to the frequency-doubled output of the second dye laser and with a wave number $\tilde{\nu}_2$ tunable in the range from 31 000 $cm^{-1}$ to 35 800 $cm^{-1}$, resonantly excites the ionic core from the selected $X^+(v'')$ state to a vibrational level ($v'$) of either of the two spin–orbit components of the $A^+$ excited state. Further photoabsorption leads to the dissociation of the molecule into a ground-state neutral Ar atom and a Mg atom in a high Rydberg state.[21]

The interaction between the MgAr molecules and the laser pulses occurs within a 5.8-cm-long stack of five equally spaced and resistively coupled cylindrical electrodes. A small electric field of ≃1.7 V/cm is applied across the stack immediately after photoexcitation and photodissociation and displaces the ions produced by the laser pulses, called prompt ions, away from the interaction region without affecting the atoms and molecules excited to Rydberg states. After ≃5 $\mu$s, a pulsed extraction field of 130 V/cm is applied to the stack to field ionize the Rydberg atoms and molecules and accelerate all positively charged particles into a linear time-of-flight region, at the end of which they are detected by a micro-channel-plate detector. The spatial separation between the prompt ions and ions generated by pulsed-field ionization prior to extraction makes it possible to distinguish them by their time of flight. By recording the yield of $Mg^+$ ions produced by delayed pulsed field ionization as a function of the wave number of the second laser, the resonance-enhanced multiphoton dissociation of the $MgAr^+$ ion core via the $A^+$ state can be recorded in a background-free manner.

## III. EXPERIMENTAL RESULTS

We have recorded the spectra of the transitions from the $X^+(v'')$ state to the $A^+_{\Omega'}(v')$ state of $^{24}MgAr^+$ with $\Omega' = 1/2$ and 3/2 and $v' = 0$–29. For each $v'$, the value of the vibrational quantum number $v''$ of the initial state was chosen so that the corresponding Franck–Condon factor was large enough for the transition to be observed. The assignment of the observed bands to the given values of $v'$ and $v''$ is based on the isotopic-shift analysis carried out in previous studies.[21,25,43] The ability to prepare the ground-state molecular ion in a broad range of selected (ro)vibrational states ($v'' = 0$–9 in the present case) is a property of the isolated-core multiphoton Rydberg-dissociation technique and is essential for observing vibrational states of the $A^+$ excited electronic state with $v'$ as high as 29. In contrast, ion-beam-based techniques are typically limited to the rotational and vibrational levels of the ground electronic state of the ion that are thermally populated in the ion source, e.g., $v'' = 0$–1 in the case of $MgAr^+$,[24,25] which limits the accessible vibrational levels of the $A^+$ state to $v' \leq 14$.[24,25]

Figures 1 and 2 show the high-resolution spectra of the $A^+_{1/2}(v' = 17) \leftarrow X^+(v'' = 3)$ and $A^+_{3/2}(v' = 17) \leftarrow X^+(v'' = 3)$ bands, respectively. Their rotational structure consists of four branches associated with transitions from the rotational levels of the $X^+$ ($^2\Sigma^+$) state, described by Hund's coupling case (b) and labeled by the quantum number $N''$ associated with the total angular momentum without spin, to rotational levels of the $A^+$ ($^2\Pi_{\Omega'}$) states, described by Hund's coupling case (a) and labeled by the quantum number $J'$ associated with the total angular momentum. In the case of the transition to the $A^+_{1/2}(v' = 17)$ level, shown in Fig. 1, the rotational structure is fully resolved except in the region of the band-head of the $\Delta_{J'N''} = J' - N'' = -0.5$ branch between 34 779.9 $cm^{-1}$ and 34 781.5 $cm^{-1}$. As in our previous work,[21] the positions of these

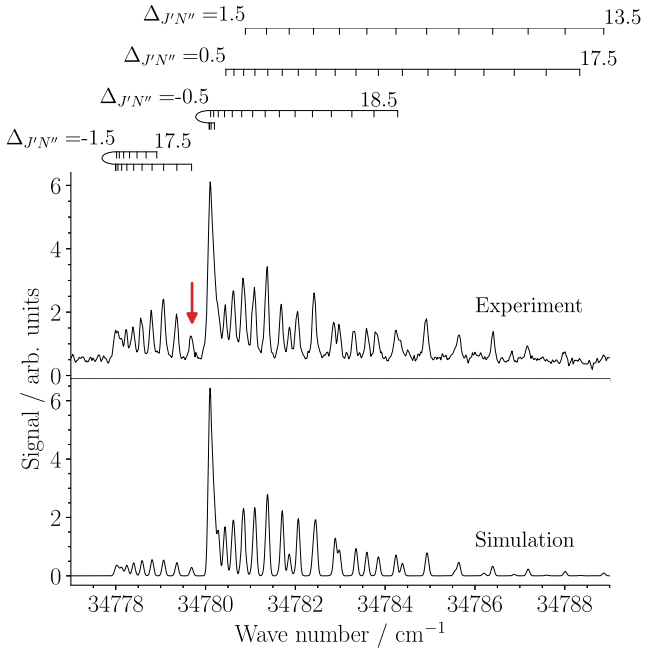


**FIG. 1**. Measured and calculated spectra of the $A^+_{1/2}(v' = 17) \leftarrow X^+(v'' = 3)$ band of $^{24}MgAr^+$. The assignment bars give the positions of the transitions to levels of the $A^+$ state of successive values of $J'$. The red arrow indicates the position of the $A^+_{1/2}(v' = 17, J' = 1/2) \leftarrow X^+(v'' = 3, N'' = 2)$ transition.

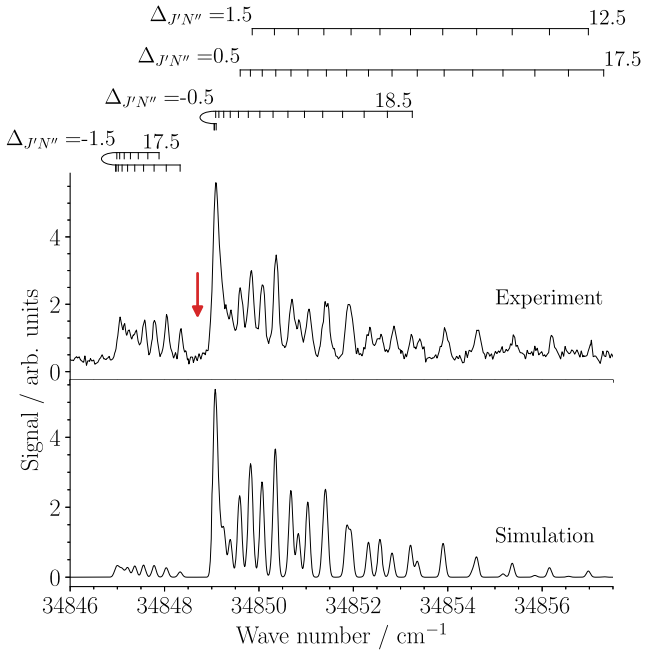


**FIG. 2**. Measured and calculated spectra of the $A^+_{3/2}(v' = 17) \leftarrow X^+(v'' = 3)$ band of $^{24}MgAr^+$. The assignment bars give the positions of the transitions to levels of the $A^+$ state of successive values of $J'$. The red arrow indicates the calculated position of the hypothetical transition $A^+_{\Omega'}(v' = 17, J' = 1/2) \leftarrow X^+(v'' = 3, N'' = 2)$. This transition is not observed, indicating that $\Omega' = 3/2$.

individual lines were determined by fitting them with Gaussian functions with a full width at half maximum of 0.1 $cm^{-1}$. The origin of the band $\tilde{\nu}_{v'v''}$ and the rotational constants $B''_{v''}$ and $B'_{v'}$ of the initial and final states, respectively, were obtained from the line positions in a least-squares fit based on the standard expression[44,45]

$$\tilde{\nu} = \tilde{\nu}_{v'v''} + B'_{v'}\left[J'(J'+1) - \Omega'^2\right] - B''_{v''}N''(N''+1). \quad (1)$$

At the low values of $N''$ and $J'$ relevant in the present experiment ($N'' \lesssim 11$, $J' \lesssim 25/2$), the effects of the centrifugal distortion on the positions of the rotational levels are negligible.

The $1\sigma$ statistical uncertainties of the band origins determined in the fit are $\Delta\tilde{\nu}_{v'v''} = 0.1$ $cm^{-1}$. They represent the standard deviation of values extracted from several independent spectra recorded under identical experimental conditions.[21] The systematic uncertainties of the band origins are 0.04 $cm^{-1}$ and correspond to the absolute accuracy of the wave-number calibration. The $1\sigma$ statistical uncertainties of the rotational constants are those resulting from the least-squares fits. The spectra displayed in the lower panel of Figs. 1 and 2 were calculated using the fit results and the rotational line strengths for transitions from a state described by Hund's coupling case (b) to a state described by Hund's coupling case (a).[45] The initial rotational states were assumed to be thermally populated at a temperature of 7 K. The agreement between the experimental and simulated spectra is excellent, with the exception of the intensities of the members of the $\Delta_{J'N''} = -1.5$ branch, which appear underestimated in the simulation. Possible reasons for this discrepancy are discussed in Ref. 21.

The assignment of the bands to particular values of $v'$ and $v''$ is known.[21,25,43] However, their attribution to $\Omega' = 1/2$ or $\Omega' = 3/2$ relied until now on the assumption that the energetic ordering of the two spin–orbit components of the $A^+$ molecular state is regular, as in the case of the $3p_j(j = 1/2, 3/2)$ states of $Mg^+$, and therefore that the levels with $\Omega' = 1/2$ are lower in energy than the corresponding ones with $\Omega' = 3/2$.[27] The spectra of the $A^+_{1/2}(v' = 17) \leftarrow X^+(v'' = 3)$ and $A^+_{3/2}(v' = 17) \leftarrow X^+(v'' = 3)$ bands shown in Figs. 1 and 2 unambiguously verify this assumption. For $\Omega' = 1/2$, the lowest possible value of $J'$ is 1/2, and the line corresponding to the transition from $N'' = 2$ to $J' = 1/2$, marked by a red arrow in Fig. 1, confirms that the final electronic state of the transition is indeed an $\Omega' = 1/2$ state. For $\Omega' = 3/2$, $J' \geq 3/2$, and the transition from $N'' = 2$ to $J' = 1/2$ cannot be observed. The wave number at which one would expect such a transition for an $\Omega' = 1/2$ final state was calculated using Eq. (1) and is marked by the red arrow in Fig. 2. The absence of a line at this position in the experimental spectrum confirms the attribution to the $\Omega' = 3/2$ final state.

The band origins $\tilde{\nu}_{v'v''}$ determined from least-squares fits of the experimental spectra recorded from the $X^+$ ground-state levels with $v'' = 3, 6, 7$, and 9 to $A^+$ levels up to $v' = 29$ are listed in Table I, along with the rotational constants of the $A^+_{1/2,3/2}(v')$ states up to $v' = 28$. In some cases, only a few isolated rotational lines could be identified. To increase the reliability of the fit results, $B''_{v''}$ was fixed to the weighted average of the values determined from other bands (see Table II). The $1\sigma$ statistical uncertainty of $B'_{v'}$ was also increased to 0.01 $cm^{-1}$ in these cases. In the case of $v' = 29$, only prominent bandheads were observed, which did not permit the determination of $B'_{29}$ for either of the two spin–orbit components. The band origins were obtained in least-squares fits of the simulated rotational contours of

**TABLE I**. Observed band origins $\tilde{\nu}_{v'v''}$ of the $A^+_{\Omega'}(v') \leftarrow X^+(v'')$ transitions. The term values $T'^{(obs)}_{v'}$ of the $A^+_{\Omega'}(v')$ levels are also given, along with the difference between these values and those extracted from available experimental data[25,27] ($\Delta T'^{(1)}_{v'}$) and those calculated using the potential-energy functions determined in this article ($\Delta T'^{(2)}_{v'} = T'^{(obs)}_{v'} - T'^{(calc)}_{v'}$). The measured rotational constants $B'^{(obs)}_{v'}$ of the $A^+_{\Omega'}(v')$ levels are also compared to the results obtained from these potential-energy functions ($\Delta B'_{v'} = B'^{(obs)}_{v'} - B'^{(calc)}_{v'}$). All values are in $cm^{-1}$. The values in parentheses represent one standard deviation in units of the last digit.

| $v'$ | $\Omega'$ | $v''$ | $\tilde{\nu}_{v'v''}$ | $T'^{(obs)}_{v'}$ | $\Delta T'^{(1)}_{v'}$ | $\Delta T'^{(2)}_{v'}$ | $B'^{(obs)}_{v'}$ | $\Delta B'_{v'}$ |
|---|---|---|---|---|---|---|---|---|
| 0 | 1/2 | 3 | 31 153.72(10) | ... | ... | ... | 0.1950(30) | 0.0001 |
| 0 | 3/2 | 3 | 31 230.71(10) | 76.99(14) | 1.09 | 0.16 | 0.1920(40) | −0.0026 |
| 1 | 1/2 | 3 | 31 419.76(10) | 266.04(14) | −1.06 | 0.08 | 0.1900(10) | −0.0024 |
| 1 | 3/2 | 3 | 31 496.07(10) | 342.35(14) | −1.95 | 0.03 | 0.1910(20) | −0.0011 |
| 2 | 1/2 | 3 | 31 679.25(10) | 525.53(14) | 0.13 | 0.02 | 0.1899(7) | 0.0001 |
| 2 | 3/2 | 3 | 31 755.17(10) | 601.45(14) | 1.35 | 0.05 | 0.1900(20) | 0.0005 |
| 3 | 1/2 | 3 | 31 932.39(10) | 778.67(14) | 0.67 | 0.03 | 0.1890(20) | 0.0018 |
| 3 | 3/2 | 3 | 32 007.78(10) | 854.06(14) | 0.16 | −0.01 | 0.1890(10) | 0.0021 |
| 4 | 1/2 | 3 | 32 179.12(10) | 1025.40(14) | 2.20 | 0.08 | 0.1841(8) | −0.0005 |
| 4 | 3/2 | 3 | 32 254.03(10) | 1100.31(14) | 1.31 | 0.02 | 0.1837(2) | −0.0005 |
| 5 | 1/2 | 3 | 32 419.32(10) | 1265.60(14) | 6.20 | 0.08 | 0.1813(2) | −0.0006 |
| 5 | 3/2 | 3 | 32 493.79(10) | 1340.07(14) | 3.67 | 0.04 | 0.1818(2) | 0.0002 |
| 6 | 1/2 | 3 | 32 653.05(10) | 1499.33(14) | 6.73 | 0.13 | 0.1800(30) | 0.0008 |
| 6 | 3/2 | 3 | 32 727.04(10) | 1573.32(14) | 6.62 | 0.07 | 0.1790(20) | 0.0002 |
| 7 | 1/2 | 3 | 32 880.17(10) | 1726.45(14) | 5.15 | 0.12 | 0.1750(10) | −0.0014 |
| 7 | 3/2 | 3 | 32 953.68(10) | 1799.96(14) | 4.86 | 0.03 | 0.1760(20) | −0.0001 |
| 8 | 1/2 | 3 | 33 100.66(10) | 1946.94(14) | 4.54 | 0.09 | 0.1730(20) | −0.0006 |
| 8 | 3/2 | 3 | 33 173.62(10) | 2019.90(14) | 5.30 | −0.10 | 0.1743(10) | 0.0010 |
| 9 | 1/2 | 3 | 33 314.54(10) | 2160.82(14) | 6.42 | 0.09 | 0.1695(10) | −0.0012 |
| 9 | 3/2 | 3 | 33 387.06(10) | 2233.34(14) | 5.84 | −0.10 | 0.1717(10) | 0.0013 |
| 10 | 1/2 | 3 | 33 521.58(10) | 2367.86(14) | 6.86 | −0.05 | 0.1684(10) | 0.0006 |
| 10 | 3/2 | 3 | 33 593.81(10) | 2440.09(14) | 6.49 | −0.09 | 0.1684(10) | 0.0009 |
| 11 | 1/2 | 3 | 33 722.03(10) | 2568.31(14) | 6.61 | −0.04 | 0.1653(10) | 0.0004 |
| 11 | 3/2 | 3 | 33 793.78(10) | 2640.06(14) | 6.26 | −0.12 | 0.1653(6) | 0.0007 |
| 12 | 1/2 | 7 | 33 602.61(10) | 2761.97(20) | 6.87 | −0.03 | 0.1637(5) | 0.0019 |
| 12 | 3/2 | 7 | 33 673.92(10) | 2833.28(20) | 6.68 | −0.11 | 0.1630(10) | 0.0015 |
| 13 | 1/2 | 7 | 33 789.43(10) | 2948.79(20) | 6.59 | −0.01 | 0.1562(8) | −0.0025 |
| 13 | 3/2 | 7 | 33 860.29(10) | 3019.65(20) | 7.95 | −0.11 | 0.1582(2) | −0.0002 |
| 14 | 1/2 | 7 | 33 969.32(10) | 3128.68(20) | 4.48 | −0.04 | 0.1540(20) | −0.0016 |
| 14 | 3/2 | 7 | 34 039.72(10) | 3199.08(20) | 6.08 | −0.17 | 0.1570(30) | 0.0017 |
| 15 | 1/2 | 3 | 34 455.40(10) | 3301.68(14) | ... | −0.01 | 0.1519(7) | −0.0005 |
| 15 | 3/2 | 3 | 34 525.47(10) | 3371.75(14) | ... | −0.05 | 0.1530(8) | 0.0010 |
| 16 | 1/2 | 3 | 34 621.38(10) | 3467.66(14) | ... | −0.02 | 0.1491(7) | 0.0001 |
| 16 | 3/2 | 3 | 34 691.06(10) | 3537.34(14) | ... | −0.04 | 0.1492(5) | 0.0005 |
| 17 | 1/2 | 3 | 34 780.38(10) | 3626.66(14) | ... | 0.02 | 0.1455(2) | −0.0002 |
| 17 | 3/2 | 3 | 34 849.64(10) | 3695.92(14) | ... | −0.02 | 0.1448(4) | −0.0006 |
| 18 | 1/2 | 3 | 34 932.30(10) | 3778.58(14) | ... | 0.03 | 0.1417(2) | −0.0005 |
| 18 | 3/2 | 3 | 35 001.21(10) | 3847.49(14) | ... | 0.04 | 0.1420(4) | 0.0001 |
| 19 | 1/2 | 3 | 35 077.15(10) | 3923.43(14) | ... | 0.07 | 0.1376(10) | −0.0010 |
| 19 | 3/2 | 3 | 35 145.69(10) | 3991.97(14) | ... | 0.09 | 0.1380(5) | −0.0003 |
| 20 | 1/2 | 7 | 34 901.78(10) | 4061.14(20) | ... | 0.08 | 0.1362(4) | 0.0012 |
| 20 | 3/2 | 7 | 34 969.91(10) | 4129.27(20) | ... | 0.06 | 0.1348(2) | 0.0001 |
| 21 | 1/2 | 7 | 35 032.34(10) | 4191.70(20) | ... | 0.06 | 0.1327(3) | 0.0014 |
| 21 | 3/2 | 7 | 35 100.24(10) | 4259.60(20) | ... | 0.16 | 0.1302(10) | −0.0008 |
| 22 | 1/2 | 6 | 35 227.25(10) | 4315.20(24) | ... | 0.12 | 0.1273(5) | −0.0001 |
| 22 | 3/2 | 6 | 35 294.82(10) | 4382.77(24) | ... | 0.21 | 0.1280(10) | 0.0008 |
| 23 | 1/2 | 6 | 35 343.73(10) | 4431.67(24) | ... | 0.28 | 0.1237(10) | 0.0002 |
| 23 | 3/2 | 6 | 35 410.79(10) | 4498.74(24) | ... | 0.16 | 0.1239(10) | 0.0007 |

**TABLE I.** (*Continued.*)

| $v'$ | $\Omega'$ | $v''$ | $\tilde{\nu}_{v'v''}$ | $T'^{(\mathrm{obs})}_{v'}$ | $\Delta T'^{(1)}_{v'}$ | $\Delta T'^{(2)}_{v'}$ | $B'^{(\mathrm{obs})}_{v'}$ | $\Delta B'_{v'}$ |
|---|---|---|---|---|---|---|---|---|
| 24 | 1/2 | 6 | 35 452.75(10) | 4540.70(24) | ... | 0.10 | 0.1195(4) | 0.0000 |
| 24 | 3/2 | 6 | 35 519.78(10) | 4607.72(24) | ... | 0.18 | 0.1191(5) | −0.0001 |
| 25 | 1/2 | 6 | 35 554.84(10) | 4642.79(24) | ... | 0.05 | 0.1161(10) | 0.0008 |
| 25 | 3/2 | 6 | 35 621.67(10) | 4709.61(24) | ... | 0.15 | 0.1154(4) | 0.0003 |
| 26 | 1/2 | 7 | 35 578.56(10) | 4737.92(20) | ... | 0.07 | 0.1096(10) | −0.0015 |
| 26 | 3/2 | 7 | 35 645.15(10) | 4804.51(20) | ... | 0.08 | 0.1097(2) | −0.0012 |
| 27 | 1/2 | 9 | 35 536.79(10) | 4825.82(24) | ... | −0.17 | 0.1080(8) | 0.0013 |
| 27 | 3/2 | 9 | 35 603.45(10) | 4892.48(24) | ... | −0.03 | 0.1080(20) | 0.0014 |
| 28 | 1/2 | 9 | 35 617.88(10) | 4906.91(24) | ... | −0.32 | 0.1040(10) | 0.0018 |
| 28 | 3/2 | 9 | 35 684.62(10) | 4973.65(24) | ... | −0.16 | 0.1050(10) | 0.0028 |
| 29 | 1/2 | 9 | 35 691.99(20) | 4981.02(30) | ... | −0.63 | ... | ... |
| 29 | 3/2 | 9 | 35 759.01(20) | 5048.04(30) | ... | −0.43 | ... | ... |

the bands to the experimental spectra after fixing the values of $B'_{29}$ to the values (0.099 $\mathrm{cm}^{-1}$ for both $\Omega' = 1/2$ and 3/2) obtained by extrapolation using the standard expression[44]

$$B'_{v'} = B_e - \alpha_e\left(v' + \frac{1}{2}\right) + \beta_e\left(v' + \frac{1}{2}\right)^2. \quad (2)$$

The values of $B_e$, $\alpha_e$ and $\beta_e$ had been fitted beforehand to the experimental values of $B'_{v'}$ with $v'$ in the range from 0 to 28, and their numerical values are listed in the supplementary material. The rotational constant of the $v'' = 9$ initial state was fixed to 0.105 $\mathrm{cm}^{-1}$, corresponding to the weighted mean of the values of $B''_9$ obtained from bands with $v' \leq 28$. The uncertainties of the origins of the $v' = 29 - v'' = 9$ bands are 0.2 $\mathrm{cm}^{-1}$, which is twice as large as the uncertainties of the other band origins.

To obtain the vibrational term values of the observed $A^+$ levels, we first determined the difference in energy $T''_{v''} - T''_3$ between the various vibrational levels of the initial $X^+$ state used to record the spectra ($v'' = 6$, 7, 9) and the $v'' = 3$ level. For that purpose, we recorded the spectra of transitions from at least two different initial levels $v''$ to the same final level $v'$ and determined the corresponding ground-state combination differences, reported in Table II along with the respective rotational constants $B''_{v''}$. The present values of the energy differences agree within the error bars with those determined from the PFI-ZEKE photoelectron spectrum of the $X^+ \leftarrow a\,^3\Pi_0$ photoionization transition.[43] The values of the rotational constants $B''_{v''}$ of the $X^+$ vibrational states were obtained as weighted averages of the values determined in the fits of individual bands. The present values for $B''_{v''}$ are in good agreement with the values derived from the potential-energy function of the $X^+$ state reported in Ref. 43.

**TABLE II.** Rotational constants $B''_{v''}$ of the $X^+(v'')$ states and observed combination differences $T''_{v''} - T''_3$ with respect to the $v'' = 3$ vibrational level, determined from the band origins $\tilde{\nu}_{v'v''}$ of $A^+_{\Omega'}(v') \leftarrow X^+(v'')$ transitions. All values are in $\mathrm{cm}^{-1}$. The values in parentheses represent one standard deviation in units of the last digit.

| $v''$ | $v'$ | $\Omega'$ | $\tilde{\nu}_{v'v''}$ | $T''_{v''} - T''_3$ |
|---|---|---|---|---|
| 3 | 11 | 3/2 | 33 793.78(10) | |
| 7 | 11 | 3/2 | 33 480.70(10) | 313.08(14) |
| 7 | 25 | 3/2 | 35 550.25(10) | |
| 6 | 25 | 3/2 | 35 621.68(10) | 241.67(20) |
| 7 | 21 | 1/2 | 35 032.34(10) | |
| 9 | 21 | 1/2 | 34 902.67(10) | 442.75(20) |

| $v''$ | $B''_{v''}$ | $B''_{v''}$ [43] |
|---|---|---|
| 3 | 0.127 27(9) | 0.128 |
| 6 | 0.116 33(30) | 0.116 |
| 7 | 0.111 32(11) | 0.112 |
| 9 | 0.106 01(30) | 0.103 |

Using the energy differences $T''_{v''} - T''_3$ discussed above, the term values of the levels of the $A^+$ state are obtained from the band origins $\tilde{\nu}_{v'v''}$ using

$$T'_{v'} = \tilde{\nu}_{v'v''} + \left(T''_{v''} - T''_3\right) - \tilde{\nu}_{03}, \quad (3)$$

as listed in Table I, where they are compared with the values reported by Pilgrim *et al.*[25] The two sets of term values differ by up to ~6 $\mathrm{cm}^{-1}$, and the differences increase with $v'$.

## IV. MODEL POTENTIALS

The present data for the $A^+$ state of $MgAr^+$ extend up to $v' = 29$ and cover more than 90% of the total depth of the interaction potentials. Combined with the data reported for the $B^+$ state,[22] which extend from the vibrational ground state to the dissociation limit, they provide a complete and detailed picture of the $(3p_\sigma, 3p_\pi)$ Rydberg complex of $MgAr^+$ and can be used to derive accurate adiabatic potential-energy functions describing the three electronic states associated with the $3p$ complex in a global fit. For that purpose, the treatment of the spin–orbit interaction between the three states is necessary.

At large internuclear distances, the three states of the $3p$ complex converge to the two $Mg^+(3p_{1/2,3/2}) + Ar(^1S_0)$ dissociation limits (see Fig. 4 in Sec. V below). In this region, the spin–orbit interaction dominates over other interactions and the states are well described by Hund's angular-momentum-coupling case (c). They are labeled by an index specifying their dissociation limit (II for $Mg^+(3p_{1/2})$ and

III for $Mg^+(3p_{3/2})$) and by $\Omega'$, the quantum number corresponding to the projection of the total electronic angular momentum onto the internuclear axis. This nomenclature yields the symbols II(1/2), III(1/2), and III(3/2) for the three electronic states of the $3p$ complex. At shorter internuclear distances, the spin–orbit interaction becomes weaker than electrostatic interactions so that the quantum numbers $\Lambda$ and $\Sigma$ associated with the projections of the orbital and spin angular momenta onto the internuclear axis become good quantum numbers. The three electronic states are well described by Hund's coupling cases (a) and (b) and are designated $A^+\,^2\Pi_{1/2}$, $A^+\,^2\Pi_{3/2}$, and $B^+\,^2\Sigma^+$, respectively. The different symbols associated with the three states of the $3p$ complex at different internuclear distances $R$ and their connection to the nomenclature $A^+_{1/2}$, $A^+_{3/2}$ $B^+$ used in this article are summarized in Table III.

A transition between Hund's coupling cases (a) or (b) and Hund's coupling case (c) takes place as the internuclear distance increases and results in a progressive mixing of the $^2\Sigma$ and $^2\Pi$ characters of the states with $\Omega' = 1/2$, caused by the increasing importance of the spin–orbit interaction. The $\Omega' = 3/2$ state remains unaffected and retains its $^2\Pi_{3/2}$ Hund's case (a) character at large $R$ values. Consequently, in order to obtain the adiabatic potential-energy functions of all three electronic states at all internuclear distances $R$, a correct description of the evolution of the spin–orbit coupling with $R$ is required.

Because the $3p$ complex of $MgAr^+$ is well isolated from other electronic states, the potential-energy functions can be described reliably using a model originally developed by Cohen and Schneider.[46] This model was used, for example, to study the transition from Hund's coupling case (a) to Hund's coupling case (c) in the electronic states of the $6p$ complex in Au–rare-gas dimers[47] and in the low-lying electronic states of the rare-gas dimer ions.[37–41] In the latter case, it is necessary to further take into account the $R$-dependence of the spin–orbit coupling constant.[40,41] In the model, the spin–orbit interaction can be written, within the adiabatic approximation and using Hund's coupling case (a) basis functions, in the following matrix form:

$$\begin{pmatrix} V_\Sigma(R) & \frac{a(R)}{\sqrt{2}} & 0 \\ \frac{a(R)}{\sqrt{2}} & V_\Pi(R) - \frac{a(R)}{2} & 0 \\ 0 & 0 & V_\Pi(R) + \frac{a(R)}{2} \end{pmatrix}. \quad (4)$$

The eigenvalues of this matrix are the adiabatic potential-energy curves of the three electronic states [II(1/2), III(1/2), and III(3/2)] of the $3p$ complex. $a(R)$ is the (positive) spin–orbit constant, and $V_\Sigma(R)$ and $V_\Pi(R)$ are the potential-energy functions of the electronic states *without* spin–orbit interaction. Along the matrix diagonal, one recognizes the potential-energy functions of the $^2\Sigma^+_{1/2}$, $^2\Pi_{1/2}$, and $^2\Pi_{3/2}$ states, respectively, the latter two being split by the spin–orbit interaction $a(R)$. The off-diagonal matrix elements couple the two states with $\Omega' = 1/2$ and are responsible for the transition to Hund's coupling case (c) at large internuclear distances, where the potential energies $V_\Sigma$ and $V_\Pi$ are almost degenerate. Consequently, the electronic states II(1/2) and III(1/2) possess mixed $\Sigma$ and $\Pi$ character, as discussed above. In the separated-atom limit, the splitting between the II(1/2) and III(1/2, 3/2) states predicted by the model is $\frac{3}{2}a(R)$ and must be equal to the $3p_{1/2} - 3p_{3/2}$ spin–orbit splitting of $Mg^+$ (91.57 $cm^{-1}$[48]), which implies that $a(R \to \infty) = 61.05\ cm^{-1}$. The $R$-dependence of $a(R)$ is *a priori* unknown. However, it was found to be well described by Morse-type functions in previous studies of the rare-gas-dimer ions.[40,41] The functional form for $a(R)$ used in the present study is described below.

In the case of the $B^+$ state, the transition from Hund's coupling case (b) to Hund's coupling case (c) is directly visible in the high-resolution spectra of the $B^+(v') \leftarrow X^+(v'' = 7)$ transitions recorded for increasing $v'$.[22] The $v' = 1$ and $v' = 14$ bands are shown as examples in the upper and lower panels of Fig. 3, respectively. The rotational structure of the $v' = 1$ band is typical of transitions between two $\Sigma$ states, characterized by the rotational quantum numbers $N''$ and $N'$, respectively, and consists of overlapping P ($\Delta_{N'N''} = -1$) and

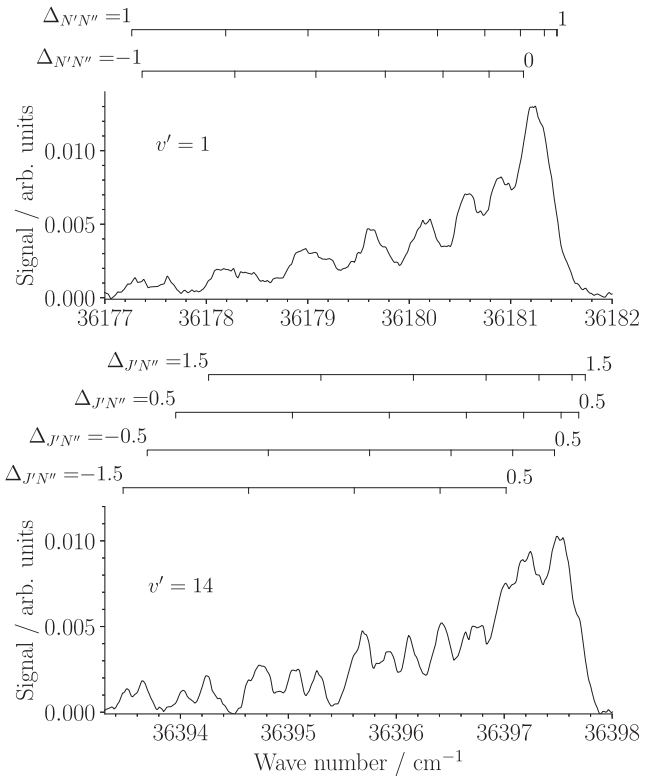


**FIG. 3.** Measured spectra of the $B^+$ ($v' = 1$) ← $X^+$ ($v'' = 7$) (top) and $B^+$ ($v' = 14$) ← $X^+$ ($v'' = 7$) (bottom) bands of $^{24}MgAr^+$. The assignment bars give the positions of the transitions to levels of the $B^+$ state of successive values of either $N'$ for $v' = 1$, described by Hund's coupling case (b), or $J'$ for $v'' = 14$, described by Hund's coupling case (c).

**TABLE III.** Summary of the various denominations of the three electronic states of the $3p$ complex of $MgAr^+$ in dependence of the internuclear distance $R$.

| State | Small $R$ | Large $R$ |
|---|---|---|
| $A^+_{1/2}$ | $^2\Pi_{1/2}$ | II(1/2) |
| $A^+_{3/2}$ | $^2\Pi_{3/2}$ | III(3/2) |
| $B^+$ | $^2\Sigma^+$ | III(1/2) |

R ($\Delta_{N'N''} = +1$) branches. These two branches are expected to overlap when the rotational constant of the final state is much smaller than that of the initial state, as in the present case (see Ref. 22 for a complete simulation of the band). The spectrum of the $v' = 14$ band consists, instead, of four distinct rotational branches, which indicates the departure of the $B^+$ state from Hund's coupling case (b). The rotational structure of the band can be well described by the four rotational branches that characterize transitions from a state described by Hund's coupling case (b) to a state described by Hund's coupling case (c). The branches are labeled $\Delta_{J'N''}$ and connect initial states with integer values of the total-angular-moment-without-spin quantum number $N''$ to final states with half-integer values of the total-angular-momentum quantum number $J'$.

The potential-energy functions $V_\Sigma(R)$ and $V_\Pi(R)$ in Eq. (4) can be represented by functions of the form

$$V_\Lambda(R) = A_\Lambda e^{-2\beta_\Lambda(R)\left(R-R_e^\Lambda\right)} - C_\Lambda e^{-\beta_\Lambda(R)\left(R-R_e^\Lambda\right)} + u_{\mathrm{LR}}^\Lambda(R), \quad (5)$$

analogous to the double-exponential/long-range (LR) model potential described by Le Roy.[36] $A_\Lambda$ and $C_\Lambda$ are obtained from the equilibrium distance $R_e^\Lambda$ and the potential-well depth $D_e^\Lambda$ using

$$A_\Lambda = D_e^\Lambda + u_{\mathrm{LR}}^\Lambda(R_e^\Lambda) + \frac{1}{\beta_\Lambda(R_e^\Lambda)} \left.\frac{\mathrm{d}u_{\mathrm{LR}}^\Lambda}{\mathrm{d}R}\right|_{R=R_e^\Lambda}, \quad (6)$$

$$C_\Lambda = 2D_e^\Lambda + 2u_{\mathrm{LR}}^\Lambda(R_e^\Lambda) + \frac{1}{\beta_\Lambda(R_e^\Lambda)} \left.\frac{\mathrm{d}u_{\mathrm{LR}}^\Lambda}{\mathrm{d}R}\right|_{R=R_e^\Lambda}, \quad (7)$$

and the function $\beta_\Lambda(R)$ is given by

$$\beta_\Lambda(R) = B_\Lambda + \sum_{i=1}^{n_\Lambda} a_i^\Lambda \left(\frac{R^5 - {R_{\mathrm{ref}}^\Lambda}^5}{R^5 + {R_{\mathrm{ref}}^\Lambda}^5}\right)^i, \quad (8)$$

with $R_e^\Lambda$, $D_e^\Lambda$, $B_\Lambda$, and $a_i^\Lambda$ being adjustable parameters of the model. In the present study, we fixed $R_{\mathrm{ref}}^\Sigma = 6.3\ a_0$ for the $\Sigma$ state and $R_{\mathrm{ref}}^\Pi = 4.3\ a_0$ for the $\Pi$ state, corresponding to values at which the least-squares fits rapidly converged. Starting from $n_\Lambda = 1$, the number $n_\Lambda$ of terms of the sum in Eq. (8) was systematically increased until agreement between the measured and calculated vibrational term values and rotational constants was reached. We found that setting $n_\Sigma = 2$ and $n_\Pi = 3$ was sufficient to reproduce the experimental results within experimental accuracy.

The long-range behavior of the potential is described by the function $u_{\mathrm{LR}}^\Lambda(R)$ [see Eq. (5)], which accounts for the dominant electrostatic interactions between $Mg^+(3p)$ and Ar,

$$u_{\mathrm{LR}}^\Lambda(R) = -\frac{\alpha_{\mathrm{Ar}}}{2R^4}\phi_\Lambda^{(4)}(R) - \frac{C_6^\Lambda}{R^6}\phi_\Lambda^{(6)}(R). \quad (9)$$

The damping functions $\phi_\Lambda^{(m)}(R)$ progressively switch off electrostatic interactions at short internuclear distances, where covalent and repulsive forces dominate. We use the damping functions

$$\phi_\Lambda^{(m)} = \left[1 - \exp\left(-3.95\frac{\rho_\Lambda R}{m} - 0.39\frac{(\rho_\Lambda R)^2}{\sqrt{m}}\right)\right]^m, \quad (10)$$

similar to the one reported by Douketis *et al.*[49] (see also Ref. 50). The system-dependent range-scaling parameters $\rho_\Lambda$ ($\Lambda = 0, 1$) represent two additional adjustable parameters of the model. In Eq. (9), $\alpha_{\mathrm{Ar}}$ is the static electric polarizability volume of the Ar atom ($\alpha_{\mathrm{Ar}} = 11.077\ {a_0}^3$[51]), and $-\alpha_{\mathrm{Ar}}/2r^4$ accounts for the charge – induced-dipole interaction in atomic units ($E_\mathrm{h}$). The term $-C_6^\Lambda/r^6$ combines three electrostatic interactions: (i) the charge – induced-quadrupole interaction, (ii) the permanent-quadrupole – induced-dipole interaction, and (iii) the dispersion interaction. These interactions must be accounted for to correctly describe the interaction potentials of the electronic states of the *np* complexes of metal–rare-gas dimers (see, e.g., Refs. 31 and 52). The only value of $C_6$ available in the literature is the estimate of Le Roy[29] for the $\Pi$ ($\Lambda = 1$) state, which does not include interaction (ii), and no value is available for the $\Sigma$ ($\Lambda = 0$) state. We have therefore re-evaluated the values of the $C_6^\Lambda$

**TABLE IV**. Parameters describing the potential-energy functions of the $A^+$ and $B^+$ states of $MgAr^+$ according to Eqs. (4), (5), (8), (10), and (12). The parameters in the upper part of the table were obtained in a weighted least-squares fit to the experimental term values and rotational constants. The parameters in the lower part of the table were left fixed during the least-squares fit. All values are in atomic units. The weighted root-mean-square deviation of the fit was 1.3.

| $V_\Sigma(R)$ | | | $V_\Pi(R)$ | | | $a(R)$ | | |
|---|---|---|---|---|---|---|---|---|
| Parameter | Value | | Parameter | Value | | Parameter | Value | |
| $R_e^\Sigma$ | 8.352 | $a_0$ | $R_e^\Pi$ | 4.526 3 | $a_0$ | H | $1.01 \times 10^{-5}$ | $E_\mathrm{h}$ |
| $D_e^\Sigma$ | 0.001 156 3 | $E_\mathrm{h}$ | $D_e^\Pi$ | 0.025 672 7 | $E_\mathrm{h}$ | S | 6.38 | ${a_0}^{-1}$ |
| $B_\Sigma$ | 0.516 4 | ${a_0}^{-1}$ | $B_\Pi$ | 0.985 02 | ${a_0}^{-1}$ | I | 0.728 | $a_0$ |
| $\rho_\Sigma$ | 0.7 | ${a_0}^{-1}$ | $\rho_\Pi$ | 0.374 2 | ${a_0}^{-1}$ | | | |
| $a_1^\Sigma$ | 0.05 | | $a_1^\Pi$ | 0.071 6 | | | | |
| $a_2^\Sigma$ | 0.22 | | $a_2^\Pi$ | 0.013 8 | | | | |
| | | | $a_3^\Pi$ | 0.082 4 | | | | |
| $R_{\mathrm{ref}}^\Sigma$ | 6.3 | $a_0$ | $R_{\mathrm{ref}}^\Pi$ | 4.3 | $a_0$ | | | |
| $C_6^\Sigma$ | 47.44 | ${a_0}^6 E_\mathrm{h}$ | $C_6^\Pi$ | 225.59 | ${a_0}^6 E_\mathrm{h}$ | | | |
| $\alpha_{\mathrm{Ar}}$ | 11.077 | $a_0^3$ | $\alpha_{\mathrm{Ar}}$ | 11.077 | $a_0^3$ | | | |

coefficients by independently calculating the contribution of each interaction according to

$$C_6^{\Lambda} = \frac{\alpha_{\mathrm{Ar}}^{(2)}}{2} + 3\Theta_{zz}^{(\Lambda)}\alpha_{\mathrm{Ar}} + C_6^{\mathrm{disp}}(\Lambda). \quad (11)$$

In Eq. (11), $\alpha_{\mathrm{Ar}}^{(2)} = 50.21\ a_0^5$ is the quadrupole polarizability of Ar,[53] and $C_6^{\mathrm{disp}}(\Lambda)$ is the Λ-dependent dispersion coefficient, calculated to be 205.5 $E_h a_0^6$ for Λ = 0 and 108.9 $E_h a_0^6$ for Λ = 1.[54] $\Theta_{zz}^{(\Lambda)}$ is the permanent quadrupole moment of $Mg^+(3p)$ for a given value of Λ, i.e., for a fixed value of the projection of the orbital angular momentum of the valence electron of $Mg^+$ onto the internuclear axis. For Λ = 1, we used the permanent quadrupole moment $\Theta_{zz}^{(1)} = 2.756\ ea_0^2$, the absolute value of which was calculated by Mitroy and Zhang.[54] From the value of $\Theta_{zz}^{(1)}$, we deduce that $\Theta_{zz}^{(0)}$, the quadrupole polarizability of $Mg^+(3p)$ for Λ = 0, is $-5.512\ ea_0^2$ (see, e.g., Ref. 55). Using Eq. (11), we obtain the values for the coefficients $C_6^{\Lambda}$ listed in Table IV.

The spin–orbit coupling constant in Eq. (4) is described by the Morse-potential-type function

$$a(R) = H\left[1 - e^{-S(R-I)}\right]^2 - H + a_{\mathrm{SO}}^{\mathrm{Mg}^+}, \quad (12)$$

where $a_{\mathrm{SO}}^{\mathrm{Mg}^+} = \frac{2}{3} \cdot 91.57\ \mathrm{cm}^{-1}$ is the $3p_{1/2} - 3p_{3/2}$ spin–orbit coupling constant in $Mg^+$.[48] The parameters $H$, $S$, and $I$ in Eq. (12) are adjustable.

In total, there are 16 adjustable parameters in the model ($R_e^{\Lambda}$, $D_e^{\Lambda}$, $B_{\Lambda}$, $\rho_{\Lambda}$, $a_1^{\Lambda}, \ldots a_{n_{\Lambda}}^{\Lambda}$, $H$, $I$, and $S$, with Λ = 0, 1) that describe the three potentials $V_i(R)$ ($i$ = 1–3) corresponding to the eigenvalues of Eq. (4). The energies associated with the rotationless vibrational levels of each potential are calculated by numerically solving the nuclear Schrödinger equation

$$\left[-\frac{1}{2\mu}\frac{\mathrm{d}^2}{\mathrm{d}R^2} + V_i(R)\right]\psi_{i,v}(R) = E_{i,v}\psi_{i,v}(R) \quad (13)$$

with a Legendre–Gauss–Lobatto discrete-variable-representation (DVR) technique.[56–59] The rotational constants $B_{i,v}$ of each vibronic energy level are calculated from the expectation value of the $1/R^2$ operator, as described in Ref. 43.

Optimal values of the 16 model parameters are determined in a weighted nonlinear least-squares fit of the calculated energies and rotational constants to the corresponding experimental values, which comprise 154 data points in total. Initial values for these parameters were obtained by fitting the model potential-energy functions to the *ab initio* potential-energy curves of the $A^+$ and $B^+$ states reported in Paper I.[22] Successive iterations were carried out during which only the parameters of either the $V_{\Pi}$, $V_{\Sigma}$, or $a(R)$ functions were varied. Once a satisfactory set of parameters was obtained, all the parameters were optimized simultaneously in a global fit. In a last step, the parameters of the $V_{\Sigma}$ potential were slightly re-optimized to reproduce the maxima and minimum of the photodissociation yield recorded above the dissociation threshold of the $B^+$ state (see Ref. 22). The relative photodissociation cross section was calculated from the $B^+$ adiabatic potential using a Legendre–Gauss–Lobatto finite-element DVR method with exterior complex scaling[57,60] and under the assumption that the electronic transition moment is independent of $R$ over the relevant range of internuclear distances. We made sure that this re-optimization had no influence on the accuracy of the potential-energy function in the region relevant for the bound states. This final step ensured that the potential describing the $B^+$ state is accurate for *both* bound states and continuum states corresponding to kinetic energy releases up to $E_{\mathrm{KER}}/(hc) \simeq 300\ \mathrm{cm}^{-1}$.

**TABLE V.** Observed band origins $\tilde{\nu}_{v'v''}$ of the $B^+(v') \leftarrow X^+(v'' = 7)$ transitions, taken from Ref. 22, term values $T_{v'}^{\prime(\mathrm{obs})}$ of the $B^+$-state levels with respect to the $A_{1/2}^+(v' = 0)$ ground vibrational level, and deviations $\Delta T_{v'}^{\prime\,(2)} = T_{v'}^{\prime(\mathrm{obs})} - T_{v'}^{\prime(\mathrm{calc})}$ of the term values calculated using the potential-energy function determined in this article. The measured rotational constants $B_{v'}^{\prime\,(\mathrm{obs})}$ of the $B^+(v')$ states are compared to the results obtained from the potential-energy function ($\Delta B_{v'}^{\prime} = B_{v'}^{\prime\,(\mathrm{obs})} - B_{v'}^{\prime\,(\mathrm{calc})}$). All values are in $\mathrm{cm}^{-1}$. The values in parentheses represent one standard deviation in units of the last digit.

| $v'$ | $\tilde{\nu}_{v'v''}$ | $T_{v'}^{\prime(\mathrm{obs})}$ | $\Delta T_{v'}^{\prime\,(2)}$ | $B_{v'}^{\prime(\mathrm{obs})}$ | $\Delta B_{v'}^{\prime}$ |
|---|---|---|---|---|---|
| 0 | 36 148.43(20) | 5307.79(26) | −0.30 | 0.0608(10) | 0.0030 |
| 1 | 36 181.34(20) | 5340.70(26) | 0.10 | 0.0550(20) | −0.0019 |
| 2 | 36 211.78(20) | 5371.14(26) | 0.05 | 0.0543(10) | −0.0015 |
| 3 | 36 240.31(20) | 5399.67(26) | 0.33 | 0.0521(10) | −0.0018 |
| 4 | 36 265.99(20) | 5425.35(26) | 0.13 | ... | ... |
| 5 | 36 289.44(20) | 5448.80(26) | 0.16 | ... | ... |
| 6 | 36 310.23(20) | 5469.59(26) | 0.02 | ... | ... |
| 7 | 36 328.53(20) | 5487.89(26) | −0.14 | 0.0420(10) | −0.0019 |
| 8 | 36 344.53(20) | 5503.89(26) | −0.16 | 0.0388(10) | −0.0018 |
| 9 | 36 358.28(20) | 5517.64(26) | −0.08 | 0.0359(10) | −0.0015 |
| 10 | 36 369.52(20) | 5528.88(26) | −0.29 | 0.0358(10) | 0.0019 |
| 11 | 36 379.13(20) | 5538.49(26) | −0.10 | 0.0324(10) | 0.0014 |
| 12 | 36 386.73(20) | 5546.09(26) | −0.09 | 0.0293(10) | 0.0018 |
| 13 | 36 392.74(20) | 5552.10(26) | −0.10 | 0.0212(10) | −0.0028 |
| 14 | 36 397.68(20) | 5557.04(26) | 0.18 | 0.0203(10) | −0.0006 |
| 15 | 36 401.25(20) | 5560.61(26) | 0.20 | 0.0187(10) | 0.0015 |
| 16 | 36 403.92(20) | 5563.28(26) | 0.23 | 0.0190(20) | 0.0044 |
| 17 | 36 405.95(40) | 5565.31(43) | 0.35 | ... | ... |
| 18 | 36 407.28(40) | 5566.64(43) | 0.35 | ... | ... |
| 19 | 36 407.80(40) | 5567.16(43) | −0.02 | ... | ... |
| 20 | 36 408.25(40) | 5567.61(43) | −0.12 | ... | ... |
| 21 | 36 408.85(40) | 5568.21(43) | 0.15 | ... | ... |

The optimal parameter values are presented in Table IV. The calculated term values and rotational constants corresponding to these parameters are compared to the experimental data obtained for the $A^+$ and $B^+$ states in Tables I and V, respectively. The vast majority of the calculated results are in agreement with experimental values within the error bars. The value of the weighted root-mean-square deviation[61] is 1.3, which indicates that the model adequately describes the experimental data.

## V. DISCUSSION

The potential-energy functions corresponding to the optimal values of the parameters are depicted in Fig. 4, where the positions of the measured vibrational energy levels are also indicated. The levels of the $A_{1/2}^+$ state are not shown for clarity. The $A_{1/2}^+$ and $A_{3/2}^+$ states are much more strongly bound ($D_e$ = 5612.1 $\mathrm{cm}^{-1}$ and 5626.6 $\mathrm{cm}^{-1}$, respectively) than the $B^+$ state ($D_e$ = 277.0 $\mathrm{cm}^{-1}$). The

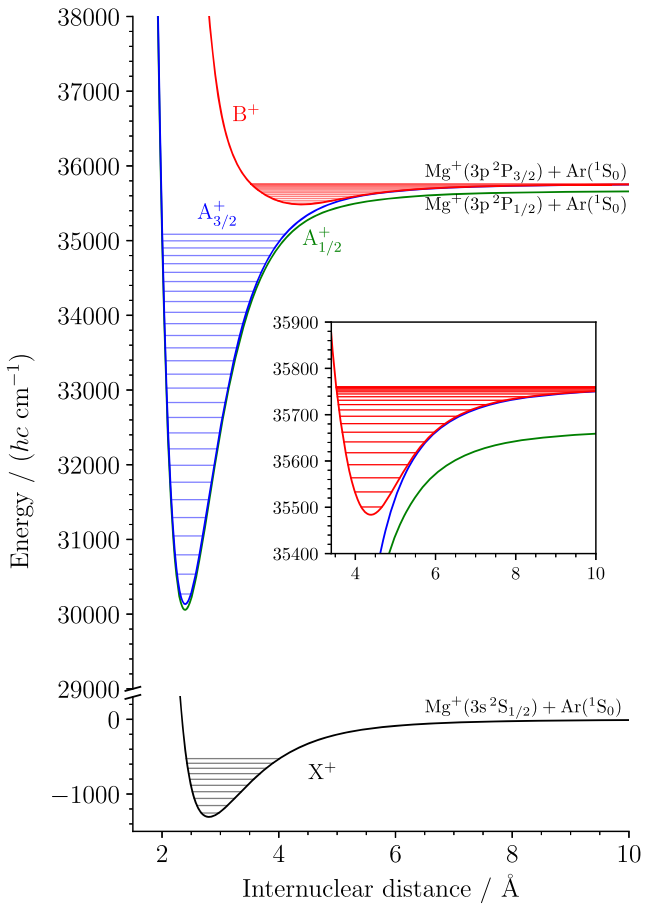


**FIG. 4.** Potential-energy curves of the first three electronic states of $^{24}$MgAr$^+$. The curve for the X$^+$ state was taken from Ref. 43. The curves of the $A^+_{\Omega'=1/2,3/2}$ and B$^+$ states were determined in the present work. The vibrational levels of the X$^+$,[43] $A^+_{\Omega'=3/2}$, and B$^+$[22] states that were observed experimentally are shown as horizontal lines. The inset shows the bound part of the B$^+$ potential-energy curve on an expanded scale.

equilibrium distances $R_e$ of the $A^+_{1/2}$ and $A^+_{3/2}$ states (4.524 $a_0$ and 4.528 $a_0$, respectively) are also significantly shorter than that of the B$^+$ state (8.289 $a_0$). The present values of both $D_e$ and $R_e$ are in good agreement with the *ab inito* calculations reported in Paper I,[22] which predict potential depths of $D_e$ = 5615.2 cm$^{-1}$, 5629.3 cm$^{-1}$, and 253.2 cm$^{-1}$ for the $A^+_{1/2}$, $A^+_{3/2}$, and B$^+$ states, respectively, and equilibrium distances of $R_e$ = 4.528 $a_0$, 4.530 $a_0$, and 8.560 $a_0$.

The reason for the large differences between the A$^+$ and B$^+$ states has already been discussed[22,24,25] and can be qualitatively understood when considering the alignment of the Mg$^+$(3$p$) orbital with respect to the internuclear axis. In the case of the A$^+$ state, the axis of the Mg$^+$(3$p_\pi$) orbital is perpendicular to the internuclear axis and leaves the Ar atom exposed to an unscreened Mg$^{2+}$ core. At large $R$, this translates into an *attractive* interaction between the permanent quadrupole moment of Mg$^+$(3$p$) and the induced dipole moment of Ar. The other dominant electrostatic interactions (charge – induced-dipole and charge – induced-quadrupole) are independent of the orbital alignment. In the case of the B$^+$ state, the axis of the $p_\sigma$ orbital is parallel to the internuclear axis and almost perfectly screens, for the Ar atom, half of the charge of the Mg$^{2+}$ core. At large $R$, this translates into a *repulsive* induced-dipole – permanent-quadrupole interaction. Moreover, because of the different alignment of the $p$ orbital, the spatial overlap of the electronic clouds of Mg$^+$ and Ar, resulting in repulsive forces, is important at larger internuclear distances for the B$^+$ state than for the A$^+$ state.

The evolution of the two spin–orbit components of the A$^+$ state from Hund's coupling case (a) to Hund's coupling case (c) is well illustrated by the evolution of the $\Omega' = 1/2 - \Omega' = 3/2$ spin–orbit splitting with $v'$, as shown in Fig. 5. At low $v'$ values, the vibrational wave function is located near the equilibrium distance $R_e(A^+_{\Omega'})$, and in this region, the $A^+\,^2\Pi_{1/2}$ state is hardly mixed with the $B^+\,^2\Sigma^+$ state because the corresponding potential-energy functions lie energetically far apart. In this case, the $A^+_{1/2} - A^+_{3/2}$ splitting is simply $a(R)$ [see diagonal elements in Eq. (4)]. The observed low-$v'$ splittings differ from $a(R \to \infty)$ = 61.05 cm$^{-1}$ because the spin–orbit constant $a(R)$ increases as $R$ decreases. At higher $v'$, the vibrational wave function extends to larger internuclear distances and is influenced by the $A^+\,^2\Pi_{1/2}$–$B^+\,^2\Sigma^+$ mixing, or equivalently by the transition from Hund's case (a) to Hund's case (c). The spin–orbit splitting increases and reaches, asymptotically, $\frac{3}{2}a(R \to \infty)$ = 91.57 cm$^{-1}$, the spin–orbit splitting of the Mg$^+$ ion. The numerical values of all spin–orbit splittings determined in this work are listed in the supplementary material.

Precise values of the dissociation energies $D_0$ of the A$^+$ and B$^+$ states can be determined from the model potentials. They are compared in Table VI to the values available in the literature. Because the experimental data for the B$^+$ state extend up to the dissociation limit and those for the A$^+$ states cover more than 90% of the total potential wells, the uncertainties on the $D_0$ values derived from the model potentials are small and estimated to be of the order of 1 cm$^{-1}$, which

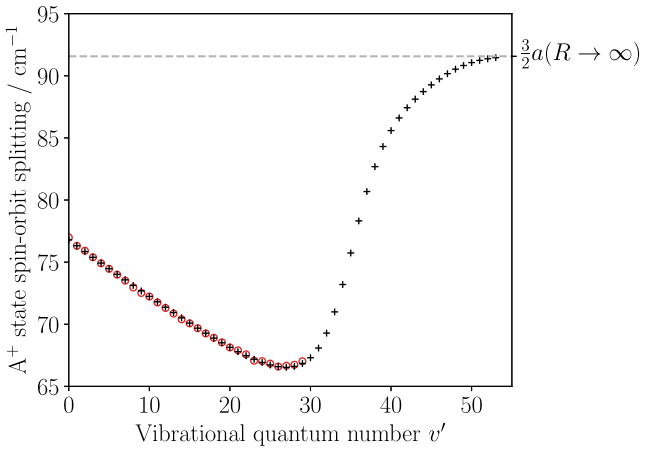


**FIG. 5.** Spin–orbit splitting between the $A^+_{1/2}(v')$ and $A^+_{3/2}(v')$ levels determined from the experimental (open circles) and calculated (crosses) term values. The limit of $\frac{3}{2}a(R \to \infty)$ = 91.57 cm$^{-1}$ is shown by the dashed gray line. It corresponds to the atomic Mg$^+$(3$p_{1/2}$–3$p_{3/2}$) spin–orbit splitting and is asymptotically reached for high vibrational levels.

**TABLE VI.** Dissociation energies $D_0$ (in $cm^{-1}$) of the $X^+$, $A^+$, and $B^+$ electronic states of $^{24}MgAr^+$ and of the a $^3\Pi_{0^-}$ state of $^{24}MgAr$ determined from the experimental data. In Ref. 29, the value of $D_0(X^+)$ was derived from $D_0(A^+)$ using a thermochemical cycle. This $D_0(X^+)$ value has been updated using the most recent experimental value of the electronic origin of the $A^+ \leftarrow X^+$ transition (see Refs. 21 and 43). The values in parentheses represent one standard deviation in units of the last digit.

| State | $D_0$ ($cm^{-1}$) | Reference |
|---|---|---|
| $A^+_{1/2}$ | 5476.7(10) | This work |
| | 5445(165) | Reference 29 |
| $A^+_{3/2}$ | 5491.5(10) | This work |
| | 5460(165) | Reference 29 |
| $B^+$ | 260.2(10) | This work |
| $X^+$ | 1246.0(12) | This work |
| | 1254(60) | Reference 43 |
| | 1214(165) | Reference 29 |
| | 1180(80) | Reference 62 |
| | 1237(40) | Reference 63 |
| a $^3\Pi_{0^-}$ | 167.6(11) | This work |
| | 160(40) | Reference 63 |

represents an improvement of more than two orders of magnitude in the uncertainties of $D_0(A^+_{1/2,3/2})$ over previously available values.[29] The present $D_0$ values for the two spin–orbit components of the $A^+$ state are in agreement within error bars with the values determined by Le Roy[29] in a near-dissociation-expansion analysis of the $v' = 0$–14 term values measured by Pilgrim *et al.*[24,25] They are significantly larger than the spin–orbit-averaged value of 2983.39 $cm^{-1}$ calculated by Gaied *et al.* using a pseudopotential approach.[34] The present $D_0$ values are in very good agreement with the *ab initio* values of 5479.4 $cm^{-1}$ and 5493.7 $cm^{-1}$ reported in Paper I for the $\Omega' = 1/2$ and 3/2 components, respectively.[22] No previous values for the dissociation energy of the $B^+$ state $D_0(B^+)$ were available in the literature before its observation in Ref. 22. The $D_0(B^+)$ value of 260.2(10) $cm^{-1}$ reported here is in reasonable agreement with the *ab initio* value of 237.7 $cm^{-1}$ reported in Ref. 22.

The dissociation energy $D_0(X^+)$ of the $X^+$ ground state of $MgAr^+$ can be calculated to be 1246.0(12) $cm^{-1}$ from the dissociation energy $D_0(B^+)$ of the $B^+$ state using the thermochemical cycle,

$$D_0(X^+) = \tilde{\nu}_{07} + T''_7 + D_0(B^+) - T(Mg^+, 3p_{3/2}). \quad (14)$$

In Eq. (14), the wave number $\tilde{\nu}_{07}$ of the $B^+(v' = 0) \leftarrow X^+(v'' = 7)$ transition is taken from Ref. 22, the term value $T''_7$ of the $X^+(v'' = 7)$ level is taken from Ref. 43, and $T(Mg^+, 3p_{3/2}) = 35\,760.88$ $cm^{-1}$ is the term value of the $3p_{3/2}$ state of $Mg^+$.[48] The present value of the dissociation energy of the $X^+$ state is compared in Table VI to other experimental values or values determined from experimental data. Our new value is in excellent agreement with the most recent ones but much more precise. It is also in agreement with the latest *ab initio* value of 1238 $cm^{-1}$ obtained by Tuttle *et al.*[35] and the value of 1235 $cm^{-1}$ calculated by Gaied *et al.*[34]

The dissociation energy of the a $^3\Pi_{0^-}$ metastable state of the neutral MgAr molecule can be determined in a similar way using

$$D_0(a) = \tilde{\nu}_{07} + \tilde{\nu}'_{70} + D_0(B^+) - \tilde{\nu}(Mg^+(3s_{1/2} - 3p_{3/2})) - E_i(Mg(3s3p\,^3P_0))/(hc), \quad (15)$$

where $E_i(Mg(3s3p^3P_0))$ is the ionization energy of the $3s3p^3P_0$ state of atomic Mg and $\tilde{\nu}'_{70}$ is the wave number of the $X^+(v'' = 7) \leftarrow$ a $(v''' = 0)$ ionizing transition[64] reported in Ref. 43. The present value of 167.6(11) $cm^{-1}$ for $D_0(a)$ is in close agreement with the value of 160(40) $cm^{-1}$ reported by Massick and Breckenridge and estimated from the results of Birge–Sponer extrapolations and *ab initio* calculations.[63]

In Paper I,[22] we showed that high-lying vibrational levels of the $B^+$ state ($v' \geq 7$) decay predominantly by spin–orbit predissociation into the $Mg^+(^2P_{1/2}) + Ar(^1S_0)$ continuum associated with the $\Omega' = 1/2$ spin–orbit component of the $A^+$ state (see inset in Fig. 4).[22] This effect can be studied theoretically with the model presented in Sec. IV by diagonalizing the part $H_{SO}$ of the Hamiltonian in Eq. (4) corresponding to the spin–orbit interaction between $\Omega' = 1/2$ states in a basis of diabatic Hund's-coupling-case-(a) vibronic functions $|v', {}^2\Lambda'_{1/2}\rangle$. In doing so, we neglect heterogeneous perturbations. The matrix elements are

$$\langle v, {}^2\Sigma_{1/2}|H_{SO}|v', {}^2\Sigma_{1/2}\rangle = 0, \quad (16)$$

$$\langle v, {}^2\Pi_{1/2}|H_{SO}|v', {}^2\Sigma_{1/2}\rangle = \int dR\, (\chi^v_\Pi(R))^* \frac{a(R)}{\sqrt{2}} \chi^{v'}_\Sigma(R), \quad (17)$$

$$\langle v, {}^2\Pi_{1/2}|H_{SO}|v', {}^2\Pi_{1/2}\rangle = -\int dR\, (\chi^v_\Pi(R))^* \frac{a(R)}{2} \chi^{v'}_\Pi(R). \quad (18)$$

The vibrational wave functions $\chi^v_\Sigma$ and $\chi^v_\Pi$ are obtained by solving the nuclear Schrödinger equation (13) for the potentials $V_\Sigma$ and $V_\Pi$, respectively. The basis set must include both bound and continuum vibrational wave functions, which we calculate using a Legendre–Gauss–Lobatto finite-element DVR technique with exterior complex scaling.[57,60] Diagonalization of the large complex-symmetric diabatic matrix yields complex eigenvalues with, for the metastable vibrational levels of the $B^+$ state ($v' = 7$–21), a real part equal to the energy of the level $E_{v'}$ and an imaginary part equal to $-\Gamma_{v'}/2$, where $\Gamma_{v'}$ is the predissociation width. The predissociation widths are found to lie in the range from 0.03 $cm^{-1}$ to 0.0003 $cm^{-1}$, depending on $v'$, which corresponds to lifetimes between 18 ns and 1.8 $\mu$s. These values agree with the experimental observations that (i) the broadening of individual lines in the measured spectra resulting from predissociation is equal to or smaller than the laser linewidth of 0.1 $cm^{-1}$ and (ii) the predissociation rate is faster than the time scale of the experiment (~5 $\mu$s).[22] The values of the calculated widths $\Gamma_{v'}$ are listed in the supplementary material. The positions of the predissociative vibrational levels of the $B^+$ state ($v' \geq 7$) calculated using either the adiabatic potential or the method just described differ by less than 0.25 $cm^{-1}$, i.e., by less than the experimental uncertainties of the measured term values. Lower-lying levels ($v' = 0$–6) differ by at most 0.4 $cm^{-1}$. Therefore, non-adiabatic corrections to the adiabatic vibrational energies are small, as expected from the fact that the weighted root-mean-square deviation of the fit (≃1.3) of the potential-energy functions described in Sec. IV is close to unity.

## VI. CONCLUSION

We reported a global study of the 3*p* Rydberg complex of the $MgAr^+$ molecular ion. Using the ICMRD technique, high-resolution spectroscopic data were obtained for the two spin–orbit components of the $A^+$ state, up to vibrational levels as high as $v' = 29$. Combined with the data reported on the $B^+$ state in Paper I,[22] they give a complete and detailed picture of the 3*p* Rydberg complex. Potential-energy functions were extracted from the experimental energies and rotational constants in a direct-potential-fit approach that included the *R*-dependent spin–orbit interaction between the three states of the complex. These potential-energy functions reproduce the positions of all observed vibrational levels of the $A^+_{1/2}$, $A^+_{3/2}$, and $B^+$ states to within less than 0.5 $cm^{-1}$.

The dissociation limits of the $B^+$ state and of the two spin–orbit components of the $A^+$ state were determined from the fitted potential-energy functions and have uncertainties of only 1 $cm^{-1}$, i.e., they are more precise compared to those obtained in previous studies by more than two orders of magnitude.[29] Dissociation energies with significantly reduced uncertainties could also be determined for the $X^+{}^2\Sigma^+$ state of $MgAr^+$ and the $a\,{}^3\Pi_{0^-}$ state of MgAr. Finally, the non-adiabatic effects caused by the spin–orbit coupling between the $B^+$ and $A^+$ states were investigated theoretically and provided results in excellent agreement with the experimental ones.[22]

The 4*s*, 3*d*, and 4*p* Rydberg complexes of $MgAr^+$ lie energetically about 30 000 $cm^{-1}$ above the 3*p* complex. Their investigation by ICMRD from the $A^+$ or $B^+$ states is underway. The 4*s* and 3*d* complexes lie in the same region of energy as charge-transfer states correlated with the $Mg(^1S_0) + Ar^+(^2P_{3/2,1/2})$ dissociation asymptotes. The investigation of these charge transfer states by ICMRD may be possible by detecting the pulsed field ionization of the Ar fragment in high Rydberg states instead of the Mg fragment in high Rydberg states as in the present work.

Such an investigation would enable the characterization of the effects of the charge-transfer interaction on the Rydberg states of molecular ions. Exciting the molecular ion even further, we expect that the ground electronic state of the doubly charged $MgAr^{2+}$ ion can be reached and investigated by pulsed-field-ionization zero-kinetic-energy (PFI-ZEKE) photoelectron spectroscopy following the procedure we recently tested with $Mg^+$.[42] This procedure is general and can be applied to molecular cations other than $MgAr^+$ in future work. The investigation of doubly charged molecular ions by high-resolution photoelectron spectroscopy would permit the exploration of the diversity and complexity of the mechanisms responsible for the stability or instability of such systems, as illustrated in Fig. 1 of Paper I[22] and discussed by Schröder and Schwarz.[65]

## SUPPLEMENTARY MATERIAL

See the supplementary material for tables listing the molecular constants of the $A^+$ and $B^+$ states, the $v$-dependent spin–orbit splittings and spin–orbit-averaged term values of the $A^+_\Omega$ states, and the calculated nonadiabatic spin–orbit-predissociation widths of the vibrational levels of the $B^+$ state.

## ACKNOWLEDGMENTS

We thank J. A. Agner and H. Schmutz for technical support and M. Reiher and S. Knecht for fruitful discussions. This work was supported financially by the Swiss National Science Foundation (Grant No. 200020-172620) and the European Research Council through an advanced grant under the European Union's Horizon 2020 Research and Innovation Programme (Grant No. 743121).

## DATA AVAILABILITY

The data that support the findings of this study are available within the article and its supplementary material.

## REFERENCES

[1] E. Miescher, J. Mol. Spectrosc. **20**, 130 (1966).
[2] E. Miescher, Can. J. Phys. **54**, 2074 (1976).
[3] R. S. Mulliken, J. Am. Chem. Soc. **88**, 1849 (1966).
[4] R. S. Mulliken, J. Am. Chem. Soc. **91**, 4615 (1969).
[5] G. Herzberg and Ch. Jungen, J. Mol. Spectrosc. **41**, 425 (1972).
[6] H. Lefebvre-Brion and R. W. Field, *The Spectra and Dynamics of Diatomic Molecules* (Elsevier, Amsterdam, 2004).
[7] J. J. Kay, S. L. Coy, B. M. Wong, Ch. Jungen, and R. W. Field, J. Chem. Phys. **134**, 114313 (2011).
[8] Ch. Jungen, in *Handbook of High-Resolution Spectroscopy*, edited by M. Quack and F. Merkt (John Wiley & Sons, Ltd., 2011).
[9] D. Sprecher, J. Liu, T. Krähenmann, M. Schäfer, and F. Merkt, J. Chem. Phys. **140**, 064304 (2014).
[10] M. Glass-Maujean, C. Jungen, A. M. Vasserot, H. Schmoranzer, A. Knie, S. Kübler, A. Ehresmann, and W. Ubachs, J. Mol. Spectrosc. **338**, 22 (2017).
[11] J. P. Maier, Int. J. Mass Spectrom. **104**, 1 (1991).
[12] L. Zhu and P. Johnson, J. Chem. Phys. **94**, 5769 (1991).
[13] K. Müller-Dethlefs and E. W. Schlag, Angew. Chem., Int. Ed. **37**, 1346 (1998).
[14] M. A. Duncan, Int. J. Mass Spectrom. **200**, 545 (2000).
[15] T. Oka, *The Encyclopedia of Mass Spectrometry* (Elsevier, Amsterdam, 2003), Vol. 1, p. 217.
[16] S. K. Stephenson and R. J. Saykally, Chem. Rev. **105**, 3220 (2005).
[17] T. Amano, in *Handbook of High-Resolution Spectroscopy*, edited by M. Quack and F. Merkt (John Wiley & Sons, Chichester, 2011), Vol. 3, pp. 1267–1289.
[18] S. Willitsch, in *Handbook of High-Resolution Spectroscopy*, edited by M. Quack and F. Merkt (John Wiley & Sons, Chichester, 2011), Vol. 3, pp. 1691–1712.
[19] F. Merkt, S. Willitsch, and U. Hollenstein, in *Handbook of High-Resolution Spectroscopy*, edited by M. Quack and F. Merkt (John Wiley & Sons, Chichester, 2011), Vol. 3, pp. 1617–1654.
[20] S. Brünken, L. Kluge, A. Stoffels, J. Pérez-Ríos, and S. Schlemmer, J. Mol. Spectrosc. **332**, 67 (2017).
[21] M. Génévriez, D. Wehrli, and F. Merkt, Mol. Phys. **118**, e1703051 (2020).
[22] D. Wehrli, M. Génévriez, S. Knecht, M. Reiher, and F. Merkt, J. Chem. Phys. **153**, 074310 (2020).
[23] R. S. Mulliken, J. Am. Chem. Soc. **86**, 3183 (1964).
[24] J. S. Pilgrim, C. S. Yeh, and M. A. Duncan, Chem. Phys. Lett. **210**, 322 (1993).
[25] J. S. Pilgrim, C. S. Yeh, K. R. Berry, and M. A. Duncan, J. Chem. Phys. **100**, 7945 (1994).
[26] C. S. Yeh, J. S. Pilgrim, K. F. Willey, D. L. Robbins, and M. A. Duncan, Int. Rev. Phys. Chem. **13**, 231 (1994).
[27] C. T. Scurlock, J. S. Pilgrim, and M. A. Duncan, J. Chem. Phys. **103**, 3293 (1995).
[28] H. Partridge, C. W. Bauschlicher, and S. R. Langhoff, J. Phys. Chem. **96**, 5350 (1992).
[29] R. J. Le Roy, J. Chem. Phys. **101**, 10217 (1994).

[30]C. W. Bauschlicher and H. Partridge, Chem. Phys. Lett. **239**, 241 (1995).
[31]K. L. Burns, D. Bellert, A. W.-K. Leung, and W. H. Breckenridge, J. Chem. Phys. **114**, 7877 (2001).
[32]D. Bellert and W. H. Breckenridge, Chem. Rev. **102**, 1595 (2002).
[33]A. M. Gardner, C. D. Withers, J. B. Graneek, T. G. Wright, L. A. Viehland, and W. H. Breckenridge, J. Phys. Chem. A **114**, 7631 (2010).
[34]W. Gaied, H. Habli, B. Oujia, and F. X. Gadea, Eur. Phys. J. D **62**, 371 (2011).
[35]W. D. Tuttle, J. P. Harris, Y. Zheng, W. H. Breckenridge, and T. G. Wright, J. Phys. Chem. A **122**, 7679 (2018).
[36]R. J. Le Roy, J. Quant. Spectrosc. Radiat. Transfer **186**, 179 (2017).
[37]A. Wüest and F. Merkt, J. Chem. Phys. **120**, 638 (2004).
[38]P. Rupper, O. Zehnder, and F. Merkt, J. Chem. Phys. **121**, 8279 (2004).
[39]A. Wüest and F. Merkt, Mol. Phys. **103**, 1285 (2005).
[40]O. Zehnder, R. Mastalerz, M. Reiher, F. Merkt, and R. A. Dressler, J. Chem. Phys. **128**, 234306 (2008).
[41]R. Mastalerz, O. Zehnder, M. Reiher, and F. Merkt, J. Chem. Theory Comput. **8**, 3671 (2012).
[42]M. Génévriez, D. Wehrli, J. A. Agner, and F. Merkt, Int. J. Mass Spectrom. **435**, 209 (2019).
[43]D. Wehrli, M. Génévriez, C. Kreis, J. A. Agner, and F. Merkt, J. Phys. Chem. A **124**, 379 (2020).
[44]G. Herzberg, *Molecular Spectra and Molecular Structure. I. Spectra of Diatomic Molecules*, 2nd ed. (Van Nostrand Reinhold Company, New York, 1950).
[45]R. N. Zare, *Angular Momentum* (John Wiley & Sons, New York, 1988).
[46]J. S. Cohen and B. Schneider, J. Chem. Phys. **61**, 3230 (1974).
[47]R. J. Plowright, A. M. Gardner, C. D. Withers, T. G. Wright, M. D. Morse, and W. H. Breckenridge, J. Phys. Chem. A **114**, 3103 (2010).
[48]A. Kramida, Yu. Ralchenko, J. Reader, and NIST ASD Team, NIST Atomic Spectra Database (ver. 5.7.1) (Online). Available: https://physics.nist.gov/asd (February 25, 2020), National Institute of Standards and Technology, Gaithersburg, MD, 2019.
[49]C. Douketis, G. Scoles, S. Marchetti, M. Zen, and A. J. Thakkar, J. Chem. Phys. **76**, 3057 (1982).
[50]R. J. Le Roy, C. C. Haugen, J. Tao, and H. Li, Mol. Phys. **109**, 435 (2011).
[51]C. Gaiser and B. Fellmuth, Phys. Rev. Lett. **120**, 123203 (2018).
[52]S. I. Panov, J. M. Williamson, and T. A. Miller, J. Chem. Phys. **102**, 7359 (1995).
[53]J. M. Standard and P. R. Certain, J. Chem. Phys. **83**, 3002 (1985).
[54]J. Mitroy and J. Y. Zhang, Eur. Phys. J. D **46**, 415 (2008).
[55]M. Medved', P. W. Fowler, and J. M. Hutson, Mol. Phys. **98**, 453 (2000).
[56]D. E. Manolopoulos and R. E. Wyatt, Chem. Phys. Lett. **152**, 23 (1988).
[57]T. N. Rescigno and C. W. McCurdy, Phys. Rev. A **62**, 032706 (2000).
[58]D. A. Telnov and S.-I. Chu, Phys. Rev. A **59**, 2864 (1999).
[59]M. Génévriez, D. Wehrli, and F. Merkt, Phys. Rev. A **100**, 032517 (2019).
[60]B. Simon, Phys. Lett. A **71**, 211 (1979).
[61]See, e.g., Ref. 43 for the definition of the weighted root-mean-square deviation used in the present work.
[62]H. Hoshino, Y. Yamakita, K. Okutsu, Y. Suzuki, M. Saito, K. Koyasu, K. Ohshimo, and F. Misaizu, Chem. Phys. Lett. **630**, 111 (2015).
[63]S. Massick and W. H. Breckenridge, Chem. Phys. Lett. **257**, 465 (1996).
[64]The wave numbers of the $X^+{}^2\Sigma^+(v'' = 7) \leftarrow a\ {}^3\Pi_0(v = 0)$ ionizing transitions of $^{24}$MgAr, $^{25}$MgAr, and $^{26}$MgAr reported in Table 1 (third column) of Ref. 43 must be corrected from 39 341.1(5) cm$^{-1}$, 39 334.7(5) cm$^{-1}$, and 39 328.8(5) cm$^{-1}$, respectively, to 39 340.5(5) cm$^{-1}$, 39 334.1(5) cm$^{-1}$, and 39 328.2(5) cm$^{-1}$. All other table entries are not affected.
[65]D. Schröder and H. Schwarz, J. Phys. Chem. A **103**, 7385 (1999).